AIAA JOURNAL
Vol. 37, No. 1, January 1999

Microfabricated Shear Stress Sensors, Part 2: Testing and Calibration

Dan Hyman,* Tao Pan,† Eli Reshotko,‡ and Mehran Mehregany§
Case Western Reserve University, Cleveland, Ohio 44106

Three designs of surface-micromachined shear stress sensors have been tested and calibrated in a continuum flow channel. The first design, for moderate shear stress conditions, is composed of passive sensors with optically determined sensitivities of 9 and 5.5 Pa/μm of floating-element deflection for two variants. The second-generation design features floating elements integrated with on-chip electronics. The deflection is thus measured with a voltage output that displays significant nonlinearities due to the limitations of drive electronics. Complete calibration of the third design was performed, as these sensors were integrated with complex active element control circuitry. These devices demonstrated a device sensitivity of 1.02 V/Pa ± 5% over a sensor range of 0.5–3.7 V.

I. Introduction

THE design and fabrication of the sensors investigated are described in Ref. 1 and use floating elements that displace against spring suspension systems when exposed to shear forces. This direct measurement of shear stress has the potential for accurate measurements because the spring restoring force is calculated from the deflection of the floating element and must counteract the shear force in a steady-state condition. Because the shear force is the shear stress operating over the area of the floating element, there exists a direct correlation between element deflection and shear stress under any flow conditions.

One difficulty in employing floating-element shear stress sensors stems from the millimeter-range thickness of boundary layers for practical wall shear stress conditions.[2] The fluid flow's influence on the floating element is very sensitive to misalignment of the surface of the element to the surrounding surface.[3] Floating elements that protrude into the fluid flow alter the flow over the sensor relative to the surrounding surface. Similarly, a recessed element would encourage boundary-layer separations at the upstream and downstream edges, also resulting in an altered flow over the face of the element. Both of these conditions can lead to spurious or inaccurate measurements. Because of these accuracy limitations, which are dependent on sensor fabrication, microfabrication techniques described in Ref. 1 are used to manufacture the sensors in this work, an example of which is shown in Fig. 1. This paper describes the effort to test and to calibrate these sensors for both mechanical and electrical characteristics.

II. Sensor Calibration Method and Model

The testing and the calibration of sensors are conducted in a high-aspect-ratio continuum channel flow. The high aspect ratio (~100) is consistent with treating the flow as two dimensional. A similar model was presented in Schmidt et al.[4,5] and Schmidt[6] for the calibration of microfabricated shear stress sensors but did not include compressibility effects, which affect the model by as much as 10% for the range of shear stresses presented in this work. Additional detail on the method presented in this section is discussed in Ref. 7.

Schematics of the first-generation flow channel developed for sensor calibration are shown in Figs. 2 and 3. A rotameter regulates gas flow from a nitrogen tank into the entrance port of the channel with atmospheric pressure at the exit. The sensor chip containing an array of sensors is inserted parallel to the fluid flow near the exit. The channel width and height are defined by a brass shim between the machined aluminum top and bottom plates, with height selected in the range of 180–300 μm. The mean free path at standard conditions is ~0.07 mm, supporting the assumption of continuum flow.

For incompressible flow, using the momentum theorem of fluid mechanics, the shear stress on the channel wall is given by

$$\tau = -\frac{b}{2}\frac{\mathrm{d}p}{\mathrm{d}x} \tag{1}$$

independent of the velocity profile. In this expression, b is the channel height and $\mathrm{d}p/\mathrm{d}x$ is the channel pressure gradient. However, because the pressure drop in the channel is a significant fraction of the inlet pressure, the channel flow must be treated compressibly.

Including a correction for compressibility, under the assumption of an isothermal channel flow, the shear stress τ on the channel wall is

$$\tau = -\frac{b}{2}\frac{\mathrm{d}p}{\mathrm{d}x}(1 - \gamma M^2) \tag{2}$$

where the pressure gradient and the mean Mach number M are evaluated at the location of the shear stress sensor. In this expression, γ is the ratio of specific heats of the channel gas (N_2 or air). The compressible flow in an isothermal channel is treated in some detail in Ref. 8. The pressure gradient in such a flow is nonuniform.

There are four pressure taps in the channel base routed through a manifold to a single commercial pressure transducer as shown in Fig. 4. To determine the pressure gradient, a second degree curve fit is made from the tap pressures:

$$p(x) = ax^2 + bx + c \tag{3}$$

and the pressure gradient is found to be

$$p'(x) = 2ax + b \tag{4}$$

where x is the distance from the sensor location to the edge of the sensor chip at which point atmospheric pressure is assumed. This pressure gradient varies with fluid flow as suggested in Fig. 5 by the three curves shown for 2-, 4-, and 6-μm deflections of the floating elements of sensors with 100-μm-long beams. The largest deflections correspond to the greatest flow and have the steepest pressure gradient, accordingly.

To determine the mean Mach number M, the velocity at the sensor location must first be calculated. The volumetric flow rate at the rotameter is measured and adjusted by the pressure ratio between the rotameter and the sensor location, then divided by the channel

Received Dec. 3, 1997; revision received July 2, 1998; accepted for publication July 13, 1998.

*Research Assistant, Department of Electrical Engineering and Computer Science, and Hughes Fellow, Hughes Research Laboratories.
†Graduate Research Assistant, Department of Electrical Engineering and Applied Physics; currently Project Manager, Advanced MicroMachines, Inc.
‡Kent H. Smith Professor of Engineering, Department of Mechanical and Aerospace Engineering. Fellow AIAA.
§George S. Dively Professor of Engineering, Department of Electrical Engineering and Computer Science.

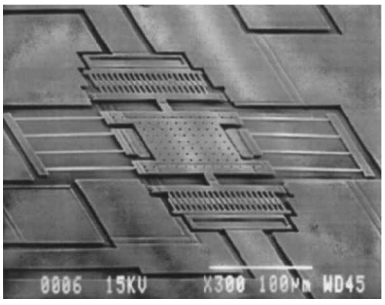

Fig. 1 Microfabricated shear stress sensor.[3]

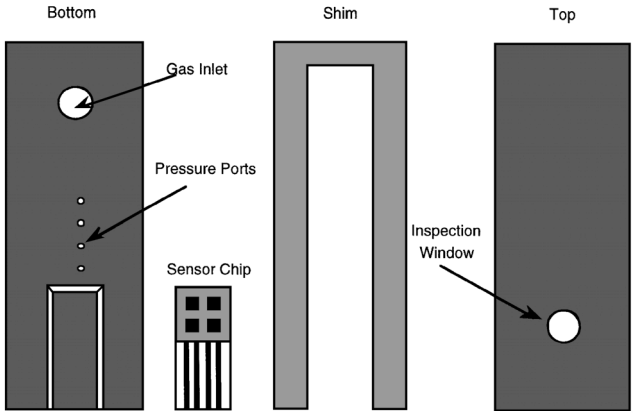

Fig. 2 Schematic of unassembled first-generation flow channel.

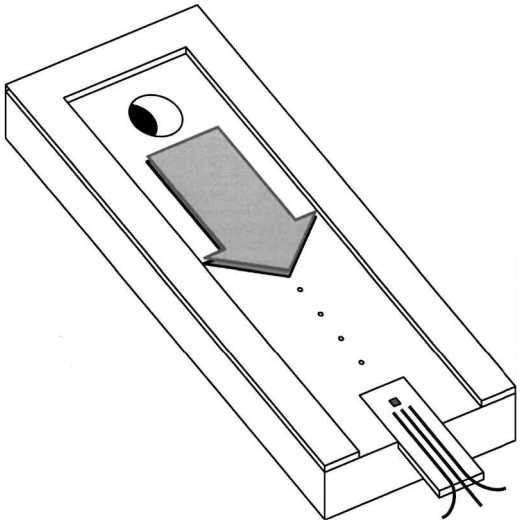

Fig. 3 Schematic of flow channel base and shim.

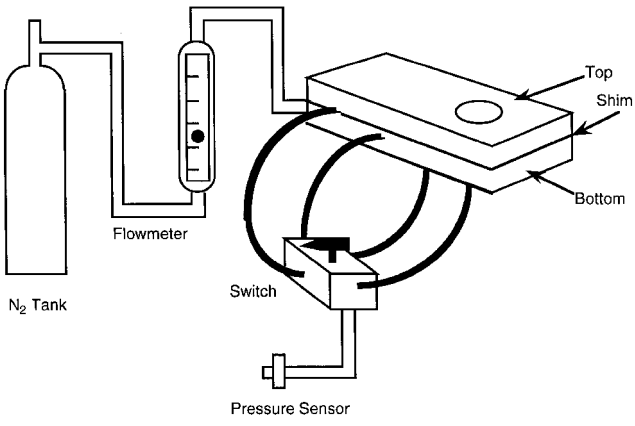

Fig. 4 First-generation flow channel with fluid monitor and delivery system assembled.

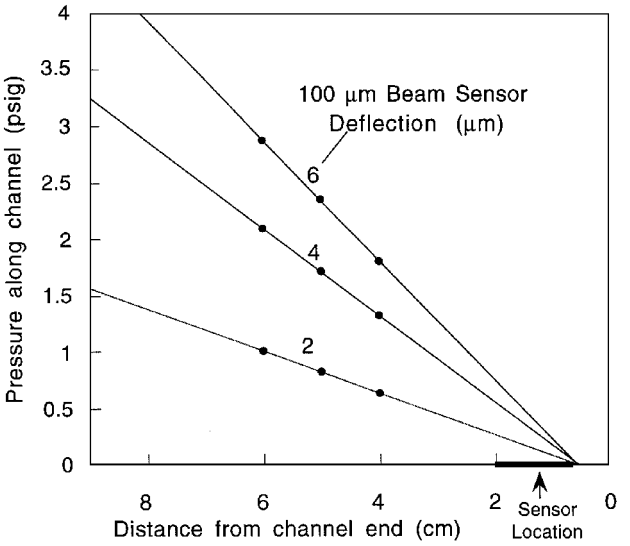

Fig. 5 Pressure along the flow channel used to interpolate the gradient.

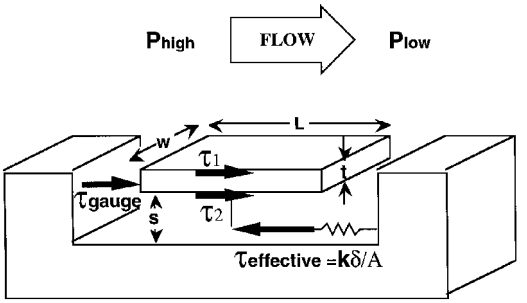

Fig. 6 Effective applied stresses on a floating element.

cross-sectional area. Dividing this velocity by the speed of sound at the channel temperature yields the mean Mach number. The Mach number at the channel exit must be kept small (< 0.25) to be remote from choking. The flow becomes choked at the condition where the fluid flow rate is limited by the channel exit conditions, which for isothermal flows occurs when $M = 1/\sqrt{\gamma}$ (Ref. 8).

The effects of the gaps between the floating element and its surrounding solid surfaces must be considered in the calibration of the shear stress sensor. The deflection of the sensing element and the restoring voltage in the case of an active sensor both depend on the total force exerted on all faces of the sensor. This also includes the pressure force on the fore and aft edge surfaces, as well as the shear force on the bottom surface of the element shown in Fig. 6. Thus, the force balance equation for the element becomes

$$F = \tau A - L\frac{\mathrm{d}p}{\mathrm{d}x}Wt - \frac{s}{2}\frac{\mathrm{d}p}{\mathrm{d}x}A \tag{5}$$

where A is the area of the floating element; L, W, and t are the length, width, and thickness of the floating element, respectively; and s is the height of the gap beneath the floating element.

The force per unit area can then be related to the channel shear stress as follows:

$$\frac{F}{A} = \tau\left\{1 + \frac{[(2t+s)/b]}{1-\gamma M^2}\right\} \tag{6}$$

where, in a typical situation, $t = s = 2$ μm and $b = 200$ μm; then because $(1-\gamma M^2) \approx 1$, the value of F/A would exceed the shear stress by about 3%.

This total stress F/A is the variable to which the sensor responds and whose sensitivity is calculated. If the same sensor is used to measure shear stress in some other flow with a different pressure gradient, then the shear stress is given by

$$\tau = \frac{F}{A} + \left(t + \frac{s}{2}\right)\frac{\mathrm{d}p}{\mathrm{d}x} \tag{7}$$

where the force F comes from the sensor calibration and the value of (dp/dx) is at the sensor location for the flow being measured. It is apparent that local pressure measurements are required for proper shear stress evaluation.

To summarize the calibration model, the actual shear stress of the fluid at the location of the sensor can be determined from Eq. (5) with the use of pressure ports along the flow path for the determination of the pressure gradient, a pressure tap at the exit of the rotameter for accurate flow speed calculation at the location of the sensor, accurate channel height measurement, and the assumptions that the models are appropriate for the flow conditions of interest.

III. Testing of First-Generation CWRU Sensors

The first-generation Case Western Reserve University (CWRU) sensors are prepared for testing with proper packaging and mounting into the sensor region of the flow channel. The sensors are affixed to flat ceramic handling substrates and inserted into the sensor mounting region of the flow channel as schematically illustrated in Fig. 3. The sensor is manually mounted flush to the channel to ± 25 μm, which is the touch-sensitive limit of the mounting procedure. The flow channel is then assembled as shown in Fig. 4.

A. Optical Testing of First-Generation CWRU Sensors

Perhaps the simplest method of measuring floating-element deflection optically locates a point on the element and compares it to a stationary reference in the field region. Figure 7 shows a magnified view of microrulers with 1-μ gaps and spaces that have been patterned into the field region with a pointer patterned into the floating element.[9] Deflection of the element under shear stress is viewed under 500× magnification, with deflections noted and compared with the calculated shear stress.

The primary disadvantages of optical measurement methods are lack of precision and limited usable conditions. Optical access to the sensor in operation must be present with a short working distance, not feasible for many wind-tunnel models or many sensors. The resolution is limited to around ± 0.3-μm accuracy, and the error and the readings themselves are user dependent. As a result, optical analysis is only suitable in calibration conditions or for verifying proper sensor operation.

The first generation of these devices was fabricated with electrical contact pads directly connected to the device. Because of the small size of the devices, capacitance changes are on the order of several femtofarads, with very small signal changes on the floating plate. With small electrical signals and characteristics, device output was lost in parasitic capacitances associated with pad contact and wire bonding. Without on-chip amplification, the weak output signals were overwhelmed by noise introduced by external measurement equipment and parasitics. These first-generation sensors were thus suitable only for optical data collection.[7]

A typical sensor response is shown in Fig. 8, which shows sensors with 100-μm beam lengths and sensitivities of 9 Pa/μm of floating-element deflection. A residual level of sticking is seen in the data for the non-CO_2 released specimen of Fig. 8, represented by a period of zero deflection at low rates of fluid flow. A certain shear stress was necessary to free the devices from the substrate before linear deflection was observed. This is indicative of the presence of a combination of sticking and friction between the floating element and the underlying substrate, a phenomenon known as stiction.

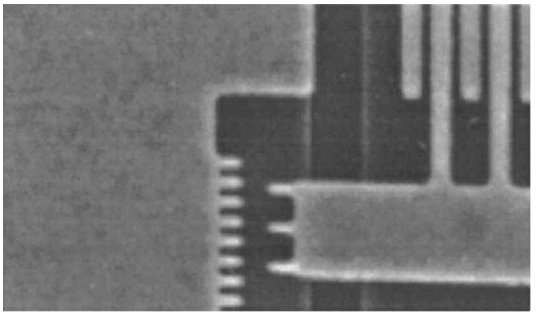

Fig. 7 Close-up of microruler for optical deflection measurement.[9]

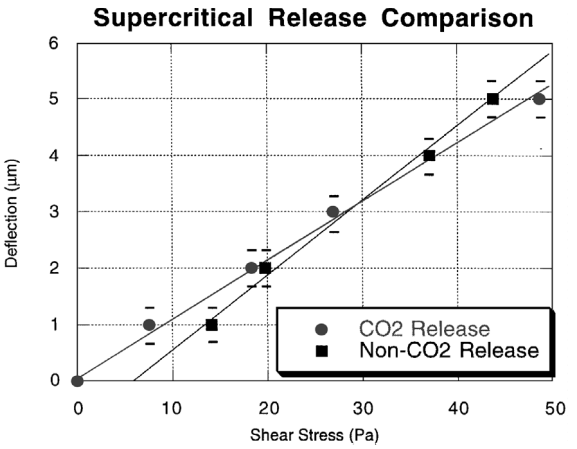

Fig. 8 Comparison between device response with and without stiction.

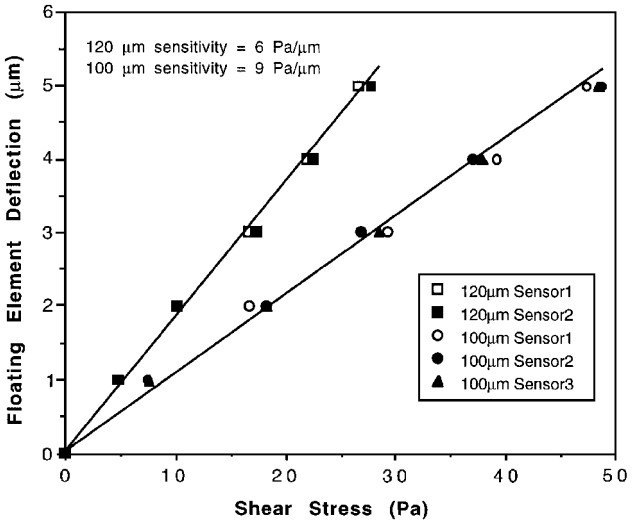

Fig. 9 Sensor deflection data for first-generation CWRU sensors of varying beam length.

Stiction is initiated in the final step of device microfabrication, where a device die is immersed in hydrofluoric acid until the sacrificial layer beneath the microstructures is etched and the devices are free to move.[10] This release is followed by immersion in deionized water to rinse the devices, which are subsequently dried with heat or compressed gas flow. Upon removal from a liquid environment, the microstructures will often adhere to the substrate. This effect has plagued microelectromechanical systems (MEMS) researchers since the development of surface micromachining, affecting devices with large geometries and flexible suspension systems, and was a leading cause of low yield and device failure for many MEMS development efforts.[11–13]

Implementing a supercritical carbon dioxide release process modeled after the work at the University of California, Berkeley,[14] a substantial increase was achieved not only in the quantity of testable microstructures but also in the quality of the data from testing those microstructures. Yield for 100-μm beam devices increased from approximately 25 to above 90%, with device failure primarily attributed to mechanical damage from handling, sawing, or agitation in the release process. Perhaps more important than the improvement of testable yield was the improvement in the device operating characteristics. Before the development of the supercritical release, the deflection characteristics of the floating-element shear stress sensors demonstrated that a finite shear force was required to overcome the stictional forces before the element deflected. Figure 8 shows that the supercritical CO_2 released specimens deflect linearly through zero.

All of the following sensors described have been released supercritically and do not demonstrate stiction. Figure 9 shows the

reproducibility of sensor operation from sensor to sensor on the same die in the same channel mounting. Although the deflection curves are close to each other for the three different sensors with 100-μm beam lengths, they differ sufficiently to require separate calibration if 1% or better accuracy is desired.

The shear force F_{shear} is linearly related to displacement with a third power relationship to the length of the beam L_b (Refs. 15 and 16):

$$\frac{4EtW_b^3}{L_b^3}\,\delta = F_{\text{shear}} \tag{8}$$

where W_b is the width of the beam, E is Young's modulus of the doped polysilicon, and t is the thickness of the folded cantilever beam structure.

The deflection characteristics of 120-μm-beam devices are compared with 100-μm-beam devices in Fig. 9. Sensitivity variation with beam length agrees with the third power relationship predicted by the mechanical model, with a 65% increase in flexibility for a 20% increase in beam length. Again, the small spread between the deflection curves suggests the need for separate calibration of each sensor. Not shown in Fig. 9 are the resonant frequencies of these sensors: 16 kHz for 100-μm-beam devices as compared with 11 kHz for 120-μm-beam devices, which is also in agreement with deflection theory.[15]

B. CWRU/Analog Devices, Inc. Sensor Testing in the Flow Channel

Sensors fabricated at Analog Devices, Inc. (ADI) were delivered packaged in hermetic 10-pin TO-100 metal can packages, the standard for the ADXL50 accelerometers upon which the sensors are based.[17] These were mounted in the flow channel by inserting them into the coverplate viewing window. Care was taken to mount the sensor surface flush with the surface of the bottom of the cover plate because small inaccuracies of either the depth or the angle of the sensor relative to the surface of the plate result in measurement error. The flow channel is assembled as described previously, external connections are made as discussed in Ref. 3, and the devices are ready for testing. The primary difference between the testing of the sensors fabricated at ADI and those at CWRU is that, instead of optical data collection, a direct voltage output is available. Optical data would prove meaningless for CWRU/ADI sensors because the sensor acts in force-balance mode and does not actually deflect under low shear stress conditions.[18]

A typical response of a CWRU/ADI shear stress sensor is shown in Fig. 10. The low end of the curve displays some slight nonlinearities that end at about 5% of full scale before the response is linear (not evident in Fig. 10). In its linear regime, the sensor shown exhibits a sensitivity of 6 Pa/V of output change. This is a typical but unreproducible value for the preamplified output of untrimmed sensors. A saturation limit is evident in Fig. 10 because of the sensor's force-balance mode of operation. At large shear stresses, the circuit cannot generate enough electrostatic forces to counter the shear forces, and the output saturates as the element deflects. The estimated electrostatic forces required to balance the shear force can be calculated given the preamplified voltages and the goemetry of the sense electrodes, but these analyses are not valid in this early work due to reproducibility problems with packaging.

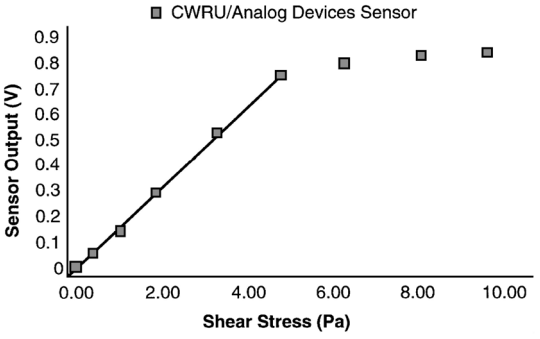

Fig. 10 Typical response of CWRU/ADI shear stress sensor.

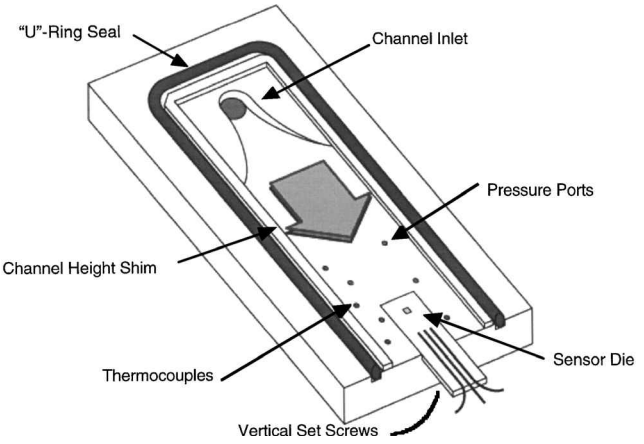

Fig. 11 Schematic of redesigned flow channel base.

Reproducibility problems were initially encountered with the CWRU/ADI sensor packaging, as the imprecision of manufacture of standard integrated circuit packages complicates the positioning of sensors parallel to the fluid flow. Slight misalignment up to 3 deg results in sensor sensitivity variations of an order of magnitude, as evident even between different mountings of the same sensor, with saturation levels are also subject to variation. Thus, a reproducible, flat packaging scheme was implemented for reliable calibration of the CWRU/ADI sensors as discussed in Sec. VI.

IV. Second-Generation Flow Channel

The first-generation flow channel was redesigned to address several problems encountered in early testing. Figure 11 shows a three-dimensional schematic of the flow channel base designed to accommodate these requirements, with only minor modification of the other flow channel elements. A metal-glass seal was replaced with an O-ring type seal to eliminate leakage along the channel edges, a primary concern in the testing of both sets of sensors. Next, in the first flow channel, the location of the pressure ports is several centimeters upstream of the actual location of the sensor, modeled after the test channel used by Schmidt et al.[4,5] and Schmidt.[6] The pressure taps in the new flow channel are located both up- and downstream of the sensor location to provide a more accurate interpolation of the pressure gradient. Their staggered placement not only allows close spacing but also enables differences between the pressure gradients to each side of the sensor to be quickly identified and corrected. This affirms the two-dimensionality of the channel flow. In addition, isothermal flow conditions previously assumed in calculations were verified with three in-line thermocouples. Finally, to eliminate output variance with the CWRU/ADI sensors, the sensor mounting region includes fine vertical adjustment set screws to enable flush sensor mounting to 25 μ.

V. Testing of Second-Generation CWRU Sensors

As discussed in Ref. 1, the second-generation sensors were fabricated in a modified n-well metal-oxide-semiconductor (NMOS) transistor process to have on-chip circuitry for signal amplification. The circuit is a differential pair amplifier with two NMOS transistors and a diode for biasing. As the process is nonstandard, characterization of the transistors is necessary to ensure functional sensor operation.

A. I-V Characteristics of Interface Circuit NMOS Transistors

Individual NMOS transistors with different W/L ratios were fabricated alongside the transducer interface circuits for transistor characterization. The I_{DS}–V_{DS} curves of a 150-μm/3-μm enhancement-mode NMOS transistor are shown in Fig. 12. These I_{DS}–V_{DS} characteristics have been tested after both a 1-min release (to expose the contact pads) and a 9-min release (to completely release the transducer elements) to evaluate the effectiveness of the circuit encapsulation. The test results showed no appreciable performance degradation after the release process. From the I_{DS}–V_{DS} characteristics, the following observations can be drawn: 1) the threshold

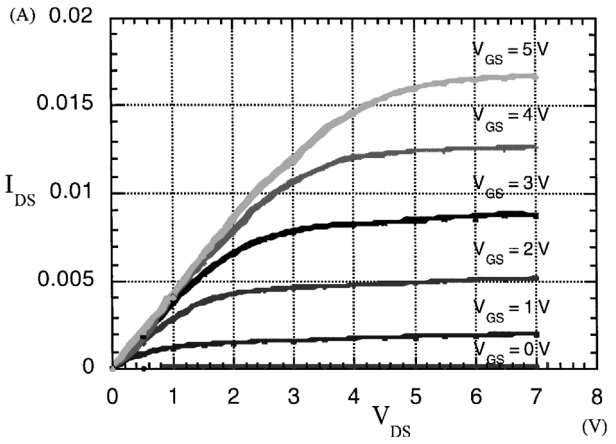

Fig. 12 I_{DS}-V_{DS} curve of a typical 150-μm/3-μm NMOS transistor.

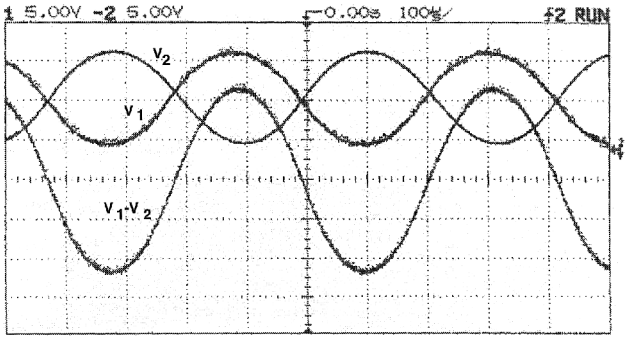

Fig. 13 Circuit configuration and output waveform of the differential pair amplifier.

voltage is very close to zero, and 2) series resistance is limiting the current. Poor probe contact could have contributed to the latter result.

The extracted threshold voltage and transconductance factors have previously been reported for these devices[19] and are not of sufficient concern to be included in the present paper. It is sufficient to mention that, given expected mobility levels of carriers, the threshold voltages and transconductance factors are reasonable and expected.

B. Characteristics of Differential Pair Amplifiers

The electronic test devices have differential pairs that have two 150-μm/3-μm MOSFETs each. The voltage outputs V_1 and V_2 and their difference are shown in Fig. 13. The best voltage gain measured was 27. A SPICE simulation yields a voltage gain of 29, which is close to the measured value.

C. Flow-Channel Testing of Second-Generation CWRU Sensors

The redesign of the CWRU sensors includes the monolithic integration of on-chip signal amplification circuitry as discussed in Ref. 1. To package the second-generation CWRU sensor dies, a bonding ceramic is positioned aft of the sensor die to minimize perturbations of the fluid flow in the region of the sensor element. The sensor is then wire bonded and inserted into the channel base as illustrated in Fig. 11, with the package and electrical lead wires extending beyond the length of the channel.

The first sensors analyzed were of the horizontal electrode type.[3] The devices were driven with the same ac signal applied to both sets of electrodes. The expected output V_0 in this case is[9]

$$V_0 = A_1 V_G = A_1 \frac{\varepsilon_0 t_{\text{poly}\,2} L}{C_p d_0} 2V_d \sin \omega t \frac{1}{1 - \left[(A/d_0 k)^{\tau}\right]^2} \qquad (9)$$

where A_1 is the voltage gain of the differential amplifier, V_G is the applied gate voltage, C_p is parasitic capacitance at the gate of M1, $t_{\text{poly}\,2}$ is the thickness of the second polysilicon layer, L is the overlap between the stationary and movable comb fingers, and d_0 is the initial gap between the comb fingers. We rewrite Eq. (9) as

$$V_0 = \frac{a}{1 - b\tau^2} \sin \omega t \qquad (10)$$

where a and b are constants determined from Eq. (9) for any driving voltage and frequency. Using an 8-kHz, 8-V peak-to-peak driving signal, the output voltage of the device was recorded with varying flow rates. The shear stress is calculated as detailed in Sec. II and plotted vs voltage output in Fig. 14. The best curve fit ($R^2 = 0.962$) gives $a = 176.4$ and $b = 0.00054$.

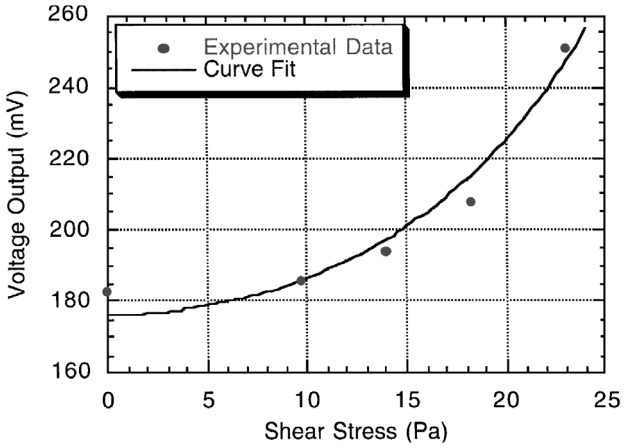

Fig. 14 Output of a second-generation CWRU horizontal-electrode shear stress sensor with synchronous driving of sense electrodes.

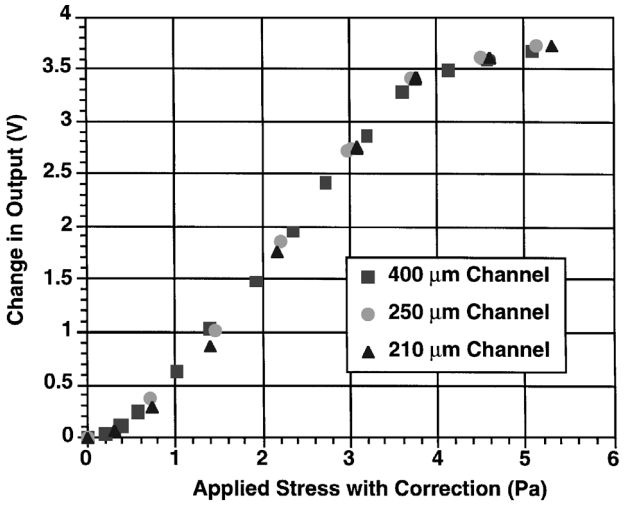

Fig. 15 Calibration curves as corrected for gauge forces and sensor underflow.

VI. Calibration of Repackaged CWRU/ADI Sensors

The full calibration of the CWRU/ADI sensors is enabled with the reproducible mounting scheme of the new package and flow channel. Custom flat bonding ceramics were developed to match height with the sensor to within 15 μm. The sensor is then wire bonded and inserted into the channel as shown in Fig. 11.

The reproducibility of the channel, device, and packaging is affirmed in Fig. 15. Trials A, B, and C have channel heights of 210, 250, and 400 μm, respectively. The sensitivity of the device is 1.03 V/Pa within the range of 0.3–3.5 V in output change. With the 200-mV offset, this corresponds to an actual output range of 0.5–3.7 V, comparable to the published range[17] of the ADI ADXL50 accelerometer of 0.2–3.8 V upon which the shear stress sensor is based. This reported output saturation is based on the full-range amplified signal rather than the preamplified feedback signal reported in Fig. 10. Because sensitivity and range are trimmed on these devices, theoretical restoring force estimates are inappropriate.

The current apparatus and calibration process introduces a number of uncertainties in device measurement including limitations in

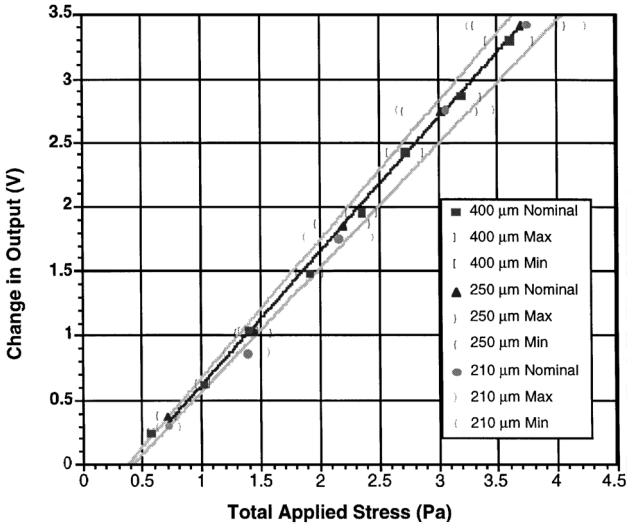

Fig. 16 Linear regime with nominal sensitivity of 1.02 ± 0.05 V/Pa.

instrument accuracy or operator-dependent uncertainties, only the greatest of which are described here.[7] The uncertainty of the optical measurement of the channel height at the exact location of the sensor is calculated to be 20 μm due to the positioning of the sensor die flush to the channel wall and the depth of field of the measurement microscope. This 20-μm out-of-the-channel height of 210, 250, or 400 μm corresponds to a fractional uncertainty of 9.5, 8.0, or 5%, respectively. The curvefits for the pressure gradients vary up to 8.5, 5.5, and 0.5% for each fit made to the pressures in the trials with channel heights of 210, 250, and 400 μm, respectively. Based on the linearity specification for the pressure transducer, these curvefits can be as inaccurate as an additional 2.1% in the slope of the line at the location of the sensor. With these and additional less-significant errors added in quadrature, the fractional uncertainty in the calculated value of shear stress in the calibration trials with channel heights of 210, 250, and 400 μm are 13.3, 10.3, and 5.4%, respectively. The data points in the linear regime of Fig. 15 are plotted with this fractional uncertainty and fitted for linear sensitivity in Fig. 16. A sensitivity of 1.02 ± 0.05 V/Pa is obtained, corresponding to a 5% calibration accuracy. Note that in Figs. 15 and 16 the sensor characteristic is properly independent of channel height.

VII. Conclusions

A surface-micromachined shear stress sensor has been developed, and sensors of varying suspension beam lengths have been calibrated in a flow channel. The sensors responded linearly to shear force as designed, with different shear stress ranges related to the different stiffnesses of the folded beams. Sensors with 100- and 120-μm-long beams, developed for moderate shear stress conditions, display sensitivities of 9 and 5.5 Pa per micrometer of floating-element deflection, respectively. When integrated with on-chip signal amplification electronics, as-fabricated NMOS measured characteristics corresponded closely to expected results, and expected nonlinear voltage output characteristics are obtained. In collaboration with ADI, an integrated shear stress sensor was fabricated with voltage output linear to shear stress. A comprehensive calibration has been performed on these sensors to give a sensitivity of 1.02 V/Pa ±5% over a range of 0.5–3.7 V.

Acknowledgments

This work was partially supported by NASA Lewis Research Center under Grant NAG3-1273. The authors thank Christopher A. Bang for the construction of the original flow channel and for the design of the floating element of the CWRU/Analog Devices integrated sensor. Technical assistance from Microfabrication Laboratory staff and Electronics Design Center staff at Case Western Reserve University is greatly appreciated. Special thanks go to Brian Willis of NASA Lewis Research Center for providing impetus and interest to shear stress sensing research.

References

[1]Pan, T., Hyman, D., Mehregany, M., Reshotko, E., and Garverick, S., "Microfabricated Shear Stress Sensors, Part 1: Design and Fabrication," *AIAA Journal*, Vol. 37, No. 1, 1999, pp. 66–72.

[2]Winter, K. G., "An Outline of the Techniques Available for the Measurement of Skin Friction in Turbulent Boundary Layers," *Progress in Aerospace Sciences*, Vol. 18, 1977, pp. 1–57.

[3]Hakkinen, R. J., "Survey of Skin Friction Measurement Techniques," AIAA Dayton-Cincinnati Section, 17th Annual Minisymposium on Aerospace Science and Technology, Dayton, OH, March 1991.

[4]Schmidt, M. A., Howe, R. T., Senturia, S. D., and Haritonidis, J. H., "Design and Calibration of a Microfabricated Floating-Element Shear-Stress Sensor," *IEEE Transactions on Electron Devices*, Vol. 35, June 1988, pp. 750–757.

[5]Schmidt, M. A., Howe, R. T., and Senturia, S. D., "A Micromachined Floating-Element Shear Sensor," *Proceedings of the 4th International Conference on Solid-State Sensors and Actuators* (Tokyo, Japan), Inst. of Electrical and Electronics Engineers, 1987, pp. 383–386.

[6]Schmidt, M. A., "Microsensors for the Measurement of Shear Forces in Turbulent Boundary Layers," Ph.D. Thesis, Dept. of Electrical Engineering and Computer Science, Massachusetts Inst. of Technology, Cambridge, MA, 1988.

[7]Hyman, D., "Testing and Calibration of Microfabricated Shear Stress Sensors," M.S. Thesis, Dept. of Electrical Engineering and Applied Physics, Case Western Reserve Univ., Cleveland, OH, May 1996.

[8]Zucrow, M. J., and Hoffman, J. D., *Gas Dynamics*, Vol. 1, Wiley, New York, 1976, pp. 273, 274.

[9]Pan, T., "Microfabricated Shear Stress Sensors," Ph.D. Thesis, Dept. of Electrical Engineering and Applied Physics, Case Western Reserve Univ., Cleveland, OH, Jan. 1996.

[10]Mehregany, M., Ko, W., Dewa, A., and Liu, C. C., *Introduction to Microelectromechanical Systems and the Multiuser MEMS Processes*, Notes from CWRU/MCNC MEMS Short Course, Case Western Reserve Univ., Cleveland, OH, 1993.

[11]Mastrangelo, C., and Hsu, C., "Mechanical Stability and Adhesion of Microstructures Under Capillary Forces," *Journal of Microelectromechanical Systems*, Vol. 2, No. 1, 1993, pp. 33–55.

[12]Alley, R. L., Cuan, G. J., Howe, R. T., and Komvopoulos, K., "The Effect of Release-Etch Processing on Surface Microstructure Stiction," *Technical Digest, IEEE Solid-State Sensors and Actuators Workshop* (Hilton Head, SC), Inst. of Electrical and Electronics Engineers, 1992, pp. 202–207.

[13]Legtenberg, R., Elders, J., and Elwenspoek, M., "Stiction of Surface Micromachined Structures After Rinsing and Drying: Model and Investigation of Adhesion Mechanism," *Technical Digest, 7th International Conference on Solid-State Sensors and Actuators* (Yokohama, Japan), Inst. of Electrical and Electronics Engineers, 1993, pp. 198–201.

[14]Mulhern, G. T., Soane, D. S., and Howe, R. T., "Supercritical Carbon Dioxide Drying of Microstructures," *Technical Digest, 7th International Conference on Solid-State Sensors and Actuators* (Yokohama, Japan), Inst. of Electrical and Electronics Engineers, 1993, pp. 296–299.

[15]Tang, W. C., Nguyen, T. H., and Howe, R. T., "Laterally Driven Polysilicon Resonant Microstructures," *Sensors and Actuators A-Physical*, Vol. 20, Nov. 1989, pp. 25–32.

[16]Tang, W. C., Nguyen, T. H., Judy, M. W., and Howe, R. T., "Electrostatic-Comb Drive of Lateral Polysilicon Resonators," *Sensors and Actuators A-Physical*, Vol. 21, No. 1–3, 1990, pp. 328–331.

[17]"Data Sheet for ADXL50 Monolithic Accelerometer with Signal Conditioning," Analog Devices, 1994.

[18]Core, T. A., Tsang, W. K., and Sherman, S. J., "Fabrication Technology for an Integrated Surface-Micromachined Sensor," *Solid State Technology*, Vol. 26, Oct. 1993, pp. 39–47.

[19]Pan, T., Melzak, J., Garverick, S., and Mehregany, M., "An Integrated Process for Smart Microstructures," *Proceedings of the SPIE Smart Structures and Materials Conference* (San Diego, CA), Society of Photo-Optical Instrumentation Engineers, 1996.

G. Laufer
Associate Editor